Full length article

Axisymmetric thermal postbuckling of functionally graded graphene nanocomposite annular plates with various geometric imperfections

Helong Wu [a,*], Ziqiang Zheng [a], Jing Guo [a], Long Li [b,*], Yumei Bao [c], Jie Yang [d]

[a] College of Mechanical Engineering, Zhejiang University of Technology, Hangzhou, 310014, China
[b] Institute of Mechanics, Chinese Academy of Sciences, Beijing, 100190, China
[c] Zhijiang College of Zhejiang University of Technology, Shaoxing, 312030, China
[d] School of Engineering, RMIT University, PO Box 71, Bundoora, VIC 3083, Australia

ARTICLE INFO

ABSTRACT

This paper presents the axisymmetric thermal postbuckling analysis of functionally graded graphene platelets-reinforced composite (FG-GPLRC) annular plates with various geometric imperfections within the framework of first-order shear deformation theory and von Kármán geometric nonlinearity. An imperfection model composed of trigonometric and hyperbolic functions is used to simulate possible imperfections with different shapes, amplitudes and locations. The 3D Halpin–Tsai model is employed to estimate the effective modulus of graphene nanocomposites. Nonlinear governing equations are derived by the variational principle and are then solved by the generalized differential quadrature method combined with the modified Newton–Raphson iteration. Parametric studies are conducted to highlight the influences of imperfection amplitude, localization degree, location and half-wave number on the thermal postbuckling behaviour of FG-GPLRC annular plates. It is found that the thermal postbuckling resistance is reduced due to the existence of geometric imperfections, and this effect become more/less significant as the imperfection amplitude/half-wave number increases.

1. Introduction

Functionally graded (FG) graphene nanocomposites are characterized by the nonuniform dispersion of graphene nanofillers along certain direction(s), and their material properties are designable and can be tailored according to application requirements [1]. Due to the low density, high strength and multifunctionality, such nanocomposites can be incorporated as high-performance lightweight structural elements in aerospace and automobile industries.

Since the pioneering works of Yang and his co-workers [2–4], extensive research efforts have been devoted to mechanical analysis of FG graphene nanocomposite structures, such as buckling, bending and vibration analyses of arches [5,6], beams [7–10], plates [11–14], as well as shells [15–17]. For the plates under in-plane loading, Song et al. [18] evaluated the buckling and postbuckling of biaxially compressed FG graphene platelet (GPL)-reinforced composite (FG-GPLRC) plates and suggested that adding a very small fraction of GPLs into polymer can significantly improve the buckling and postbuckling load-carrying capacity. Wu et al. [19] investigated the buckling and postbuckling of FG-GPLRC plates undergoing a uniform temperature rise and found that dispersing more GPLs near the outer layers leads to the highest thermal buckling and postbuckling resistance. Nguyen et al. [20] extended this

work by considering diverse through-thickness and surface temperature variations. Shakouri and Mohseni [21] carried out the buckling analysis of sandwich plates with FG-GPLRC face sheets based on the Fourier series and Navier method. Shen et al. [22,23] using a two-step perturbation approach examined the buckling and postbuckling of simply supported FG graphene-reinforced composite (FG-GRC) laminated plates subjected to mechanical and thermal loadings. Based on the isogeometric finite element formulation, Kiani [24] further analysed the thermal buckling and postbuckling of FG-GRC plates with different boundary conditions.

Annular plates are one of the essential structural elements that are widely used in many engineering systems such as aircraft, vessels, automobile and other vehicles. The study on mechanical behaviour of FG graphene nanocomposite annular plates is of great importance for their practical applications. Yang et al. [25] and Liu et al. [26] studied the linear bending and free vibration, respectively, of FG-GPLRC annular plates within the framework of three-dimensional (3D) elasticity theory. Wu et al. [27] presented the nonlinear vibration analysis of FG-GPLRC annular plates in thermal environments based on the first-order shear deformation theory (FSDT). Malekzadeh et al. [28] analysed the linear free vibration of FG-GPLRC eccentric annular plates with piezoelectric layers, while Yang et al. [29] investigated the axisymmetric vibration and thermal buckling of the same annular plates

Abbreviations and notations

2D, 3D	two-dimensional and three-dimensional
C, H	clamped and hinged supports
FG	functionally graded
FSDT	first-order shear deformation theory
Gi, Li	global and localized geometric imperfections
GDQ	generalized differential quadrature
GPL	graphene platelet
GPLRC	graphene platelet-reinforced composite
X, U, O	distribution patterns of GPLs
a, b, c	parameters defining the localization degree, location, and half-wave number of geometric imperfections
$a_{GPL}, b_{GPL}, t_{GPL}, d_{GPL}$	length, width, thickness and average diameter of GPLs
h	thickness of the annular plate
$l_j(r)$	Lagrange interpolation polynomials
r, θ, z	cylindrical coordinate system
$\alpha, \alpha_{GPL}, \alpha_m$	thermal expansion coefficient of GPLRC, GPL and epoxy matrix
γ_{rz}	shear strain component
$\varepsilon_{rr}, \varepsilon_{\theta\theta}$	normal strain components in r and θ directions
κ	shear correction factor
λ_T	buckling temperature parameter
ν, ν_{GPL}, ν_m	Poisson's ratio of GPLRC, GPL and epoxy matrix
ξ_i	GPL shape factors
ρ, ρ_{GPL}, ρ_m	mass density of GPLRC, GPL and epoxy matrix
σ_{rz}	shear stress component
$\sigma_{rr}, \sigma_{\theta\theta}$	normal stress components in r and θ directions
ψ	transverse normal rotation about the θ-axis
Π_s	strain energy of the annular plate
A	mid-plane area of the annular plate
A_0	dimensionless imperfection amplitude
A_{ij}, D_{ij}	extensional and bending stiffness components
$C_{ij}^{(m)}$	mth-order GDQ weighting coefficients
E, E_{GPL}, E_m	elastic modulus of GPLRC, GPL and epoxy matrix
E_{ii}	in-plane and out-of-plane elastic moduli of unidirectional lamina
$M_{rr}, M_{\theta\theta}$	moment resultants about θ and r axes
$M_{rr}^T, M_{\theta\theta}^T$	thermally induced moments about θ and r axes
N, N_L	number of GDQ grid points and GPLRC layers

$N_{rr}, N_{\theta\theta}$	in-plane force resultants in r and θ directions
$N_{rr}^T, N_{\theta\theta}^T$	thermally induced in-plane forces in r and θ directions
Q_{ij}	elastic stiffness components
$R_a, R_b,$	outer and inner radii of the annular plate
$\Delta T, \Delta T_{cr}$	temperature rise and critical buckling temperature rise
U, W	radial and transverse displacement components
V_{GPL}, V_m	volume fraction of GPL and epoxy matrix
V_{GPL}^*	total volume fraction of GPL
W^*	geometric imperfection
W_{GPL}	weight fraction of GPL
d	unknown displacement vector
$\mathbf{K}_L, \mathbf{K}_T$	linear stiffness and geometric stiffness matrices
$\mathbf{K}_{NL1}, \mathbf{K}_{NL2}$	nonlinear stiffness matrices
R	load vector resulting from temperature rise

structures [32–34]. On the other hand, previous studies on FG graphene nanocomposites assumed that graphene nanofillers are either unidirectionally aligned or randomly oriented in the plane (2D-random). This is, however, not often the real case that graphene nanofillers are randomly oriented and dispersed in three dimensions (3D-random) due to the constrains of manufacture technology. As a result, the elastic modulus of graphene nanocomposites is markedly overestimated with respect to the experimental values [35].

Motivated by the above issues, this paper investigates the axisymmetric thermal postbuckling of FG-GPLRC annular plates with various geometric imperfections. The elastic modulus of graphene nanocomposites is evaluated by using the 3D Halpin–Tsai model that takes into account the 3D-random orientation of GPLs in the matrix. Governing equations with geometric imperfection related terms are deduced by the variational principle and discretized according to the generalized differential quadrature (GDQ) method. The thermal postbuckling equilibrium paths of geometrically imperfect FG-GPLRC annular plates are determined by the modified Newton–Raphson iteration technique. Parametric studies are carried out to evaluate the effects of GPL distribution pattern, concentration and dimension, imperfection mode, amplitude, location and localization degree, plate geometry, and boundary conditions on the thermal postbuckling behaviour of geometrically imperfect FG-GPLRC annular plates. Thermal buckling and postbuckling results of perfect annular plates are also presented for a comparison study.

2. Theoretical formulation

2.1. FG-GPLRC annular plate

As shown in Fig. 1, an FG-GPLRC annular plate of thickness h, outer radius R_a and inner radius R_b is defined in a cylindrical coordinate system (r, θ, z). The coordinate origin is located at the centre of the plate mid-plane ($z = 0$), and the r, θ and z axes are along the radial, circumferential and thickness directions, respectively.

The annular plate is made of multiple GPLRC layers of equal thickness in which GPL nanofillers are randomly oriented and uniformly dispersed, but the GPL volume fraction changes from layer to layer according to the following patterns [9]:

Pattern X: $V_{GPL}^{(k)} = 2V_{GPL}^* |2k - N_L - 1| / N_L,$ (1)

Pattern U: $V_{GPL}^{(k)} = V_{GPL}^*,$ (2)

without eccentricity. Zheng et al. [30] examined the asymmetric stability of FG-GPLRC annular plates subjected to thermal loading. Yang et al. evaluated the asymmetric thermal buckling and postbuckling of rotating FG-GPLRC annular plates resting on an elastic foundation [31].

It should be mentioned that all these studies are restricted to the perfectly flat annular plates only and the effects of initial geometric imperfections are not taken into account. In practice, initial geometric imperfections often occur during the fabrication or service process, and may have important influences on the mechanical behaviours of
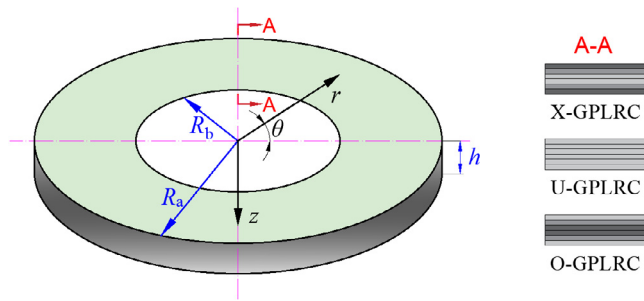
Fig. 1. Configuration and coordinate system of an FG-GPLRC annular plate.

Pattern O: $V_{\mathrm{GPL}}^{(k)} = 2V_{\mathrm{GPL}}^* \left(1 - |2k - N_{\mathrm{L}} - 1| / N_{\mathrm{L}}\right),$ (3)

where N_{L} is the total number of layers, $V_{\mathrm{GPL}}^{(k)}$ and V_{GPL}^* are the GPL volume fraction in the kth layer and the whole plate, respectively. V_{GPL}^* is related to the total GPL weight fraction W_{GPL} by

$$V_{\mathrm{GPL}}^* = \frac{W_{\mathrm{GPL}}}{W_{\mathrm{GPL}} + \left(\rho_{\mathrm{GPL}}/\rho_{\mathrm{m}}\right)\left(1 - W_{\mathrm{GPL}}\right)}, \quad (4)$$

in which ρ_{GPL} and ρ_{m} are mass densities of the GPL and matrix, respectively.

2.2. Effective material properties

In practice, graphene nanofillers are 3D-randomly oriented and dispersed in the matrix due to the constrains of manufacture technology. Consequently, the widely used 2D Halpin–Tsai model often overestimates the elastic modulus of graphene nanocomposites when compared with experimental measurements. In order to consider the 3D-random orientation of GPLs, the 3D Halpin–Tsai model is introduced to evaluate the effective elastic modulus of GPLRCs [35]:

$$E = 0.184E_{11} + 0.306E_{22} + 0.510E_{33}, \quad (5)$$

where E_{11} and E_{22} are in-plane elastic moduli, and E_{33} the out-of-plane elastic modulus of a unidirectional lamina and are determined by the Halpin–Tsai equation as [36]

$$E_{ii} = \frac{1 + \xi_i \eta_i V_{\mathrm{GPL}}}{1 - \eta_i V_{\mathrm{GPL}}} E_{\mathrm{m}}, \qquad \eta_i = \frac{E_{\mathrm{GPL}} - E_{\mathrm{m}}}{E_{\mathrm{GPL}} + \xi_i E_{\mathrm{m}}}, \quad (i = 1, 2, 3). \quad (6)$$

In the above equation, E_{GPL} and E_{m} are elastic moduli of GPLs and matrix, respectively. ξ_i is the GPL shape factor, which are defined as [37]

$$\xi_1 = 2a_{\mathrm{GPL}}/3t_{\mathrm{GPL}}, \qquad \xi_2 = 2b_{\mathrm{GPL}}/3t_{\mathrm{GPL}}, \qquad \xi_3 = 2. \quad (7)$$

where a_{GPL}, b_{GPL} and t_{GPL} denote the length, width and thickness of rectangular GPL reinforcements. For nanocomposites reinforced with circular GPLs ($E_{11} = E_{22}$ and $\xi_1 = \xi_2$), Eqs. (5) and (7) are separately reduced to

$$E = 0.49E_{11} + 0.51E_{33}, \quad (8)$$

$$\xi_1 = 2d_{\mathrm{GPL}}/3t_{\mathrm{GPL}}, \qquad \xi_3 = 2. \quad (9)$$

The other material properties of GPLRCs are calculated by the rule of mixture as

$$\alpha = \alpha_{\mathrm{m}} V_{\mathrm{m}} + \alpha_{\mathrm{GPL}} V_{\mathrm{GPL}}, \quad (10)$$

$$\nu = \nu_{\mathrm{m}} V_{\mathrm{m}} + \nu_{\mathrm{GPL}} V_{\mathrm{GPL}} \quad (11)$$

in which α, ν and V denote the thermal expansion coefficient, Poisson's ratio and volume fraction in order, with subscripts "GPL" and "m" representing GPL and matrix, respectively. V_{m} and V_{GPL} are related by $V_{\mathrm{m}} + V_{\mathrm{GPL}} = 1$.

2.3. Governing equations

Let us consider an FG-GPLRC annular plate that is stress-free at the reference temperature T_0 and then is subjected to a temperature rise ΔT. The axisymmetric problem is considered in present study, thus the circumferential displacement is neglected. Based on the FSDT and von Kármán geometric nonlinearity, the strain components are given as

$$\varepsilon_{rr} = U_{,r} + z\psi_{,r} + \frac{1}{2}\left(W_{,r}\right)^2 + W_{,r}W_{,r}^*, \qquad \varepsilon_{\theta\theta} = \frac{U}{r} + z\frac{\psi}{r}, \qquad \gamma_{rz} = W_{,r} + \psi, \quad (12)$$

where U and W are radial and transverse displacement components of an arbitrary point in the mid-plane ($z = 0$), ψ the transverse normal rotation about the θ-axis. A comma followed by subscripts denotes the partial derivative with respect to the variable r. W^* is the initial geometric imperfection in the form of the product of trigonometric and hyperbolic functions as

$$W^* = A_0 R \sec\left[a\left(\frac{r - R_{\mathrm{b}}}{R_{\mathrm{a}} - R_{\mathrm{b}}} - c\right)\right] \cos\left[b\pi\left(\frac{r - R_{\mathrm{b}}}{R_{\mathrm{a}} - R_{\mathrm{b}}} - c\right)\right] \quad (13)$$

in which A_0 is the dimensionless imperfection amplitude, $R = h/2\sqrt{3}$ the radius of gyration. Parameters a, b, and c define the localization degree, location, and half-wave number of the geometric imperfection in the radius direction. Some global (G) and localized (L) imperfections with different parameter values, together with their cross-sectional profiles, are shown in Table 1.

The linear stress–strain relationships of the annular plate including the thermal effect are expressed as

$$\sigma_{rr} = Q_{11}\varepsilon_{rr} + Q_{12}\varepsilon_{\theta\theta} - \alpha\Delta T, \qquad \sigma_{\theta\theta} = Q_{12}\varepsilon_{rr} + Q_{22}\varepsilon_{\theta\theta} - \alpha\Delta T,$$

$$\sigma_{rz} = \kappa Q_{55}\gamma_{rz}, \quad (14)$$

where the shear correction factor $\kappa = \pi^2/12$; the elastic stiffness components Q_{ij} are defined as

$$Q_{11} = Q_{22} = \frac{E}{1 - \nu^2}, \qquad Q_{12} = \frac{\nu E}{1 - \nu^2}, \qquad Q_{55} = \frac{E}{2(1 + \nu)}. \quad (15)$$

The strain energy Π_{S} of the annular plate is given by

$$\Pi_{\mathrm{S}} = \frac{1}{2}\int_A \int_{-h/2}^{h/2} \left(\sigma_{rr}\varepsilon_{rr} + \sigma_{\theta\theta}\varepsilon_{\theta\theta} + \tau_{xz}\gamma_{xz}^2\right) \mathrm{d}z\mathrm{d}A, \quad (16)$$

where A is the mid-plane area of the annular plate. By virtue of the variational principle, governing equations of the FG-GPLRC annular plate can be obtained as [27]

$$N_{rr} + rN_{rr,r} - N_{\theta\theta} = 0, \quad (17)$$

$$N_{rr}\left(W_{,r} + W_{,r}^*\right) + rN_{rr,r}\left(W_{,r} + W_{,r}^*\right) + rN_{rr}\left(W_{,rr} + W_{,rr}^*\right) + Q_{rz} + rQ_{rz,r} = 0, \quad (18)$$

$$M_{rr} + rM_{rr,r} - M_{\theta\theta} - rQ_{rz} = 0, \quad (19)$$

in which the force (N_{rr}, $N_{\theta\theta}$, Q_{rz}) and moment (M_{rr}, $M_{\theta\theta}$) resultants are given as

$$N_{rr} = A_{11}U_{rr} + \frac{1}{2}A_{11}\left(W_{,r}\right)^2 + A_{11}W_{,r}W_{,r}^* + A_{12}\frac{U}{r} - N_{rr}^{\mathrm{T}}, \quad (20)$$
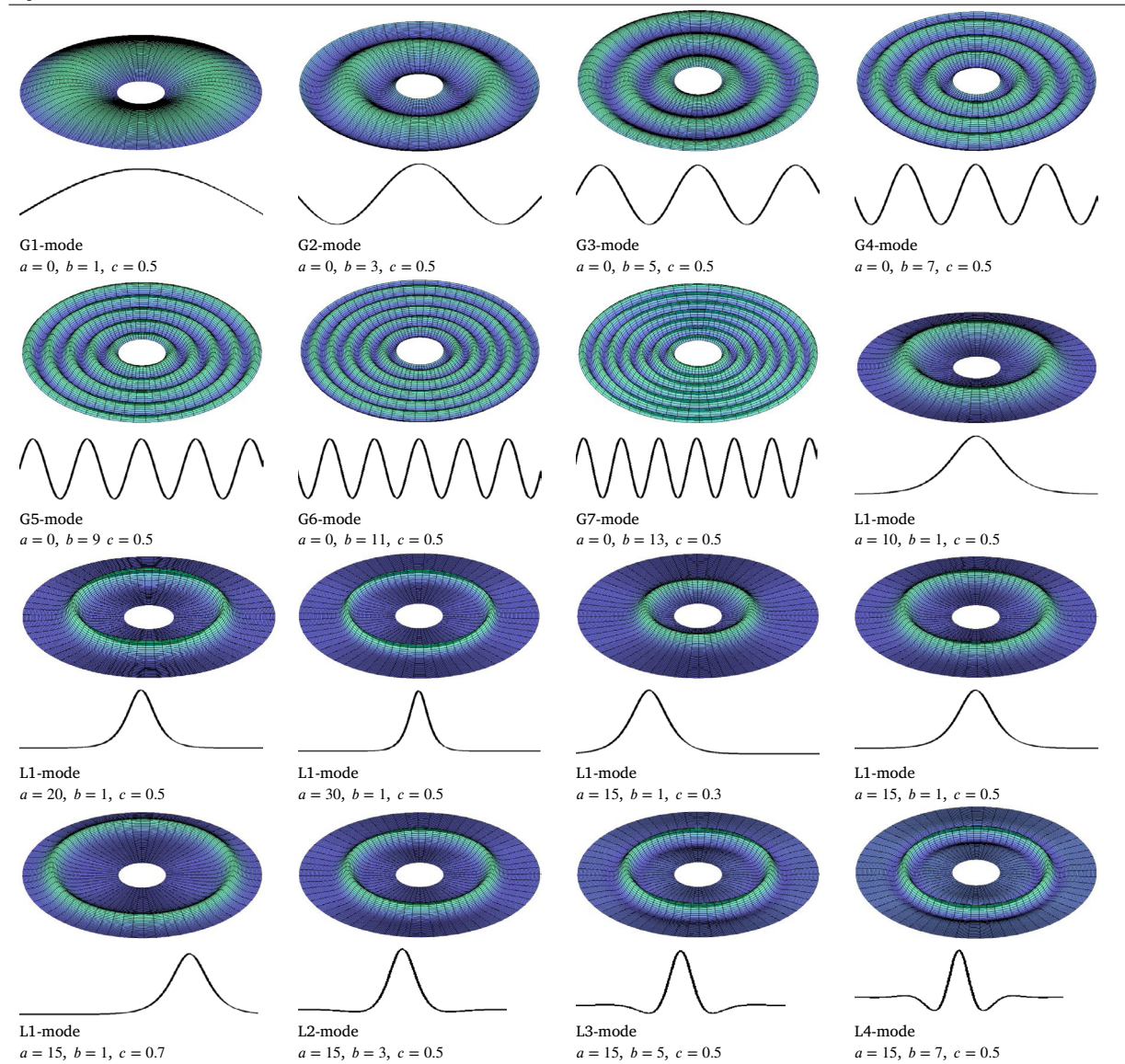
$$N_{\theta\theta} = A_{12}U_{rr} + \frac{1}{2}A_{12}\left(W_{,r}\right)^2 + A_{12}W_{,r}W_{,r}^* + A_{22}\frac{U}{r} - N_{\theta\theta}^{\mathrm{T}}, \quad (21)$$

$$Q_{rz} = \kappa A_{55}\left(W_{,r} + \psi\right), \quad (22)$$

$$M_{rr} = D_{11}\psi_{,r} + D_{12}\frac{\psi}{r} - M_{rr}^{\mathrm{T}}, \quad (23)$$

$$M_{\theta\theta} = D_{12}\psi_{,r} + D_{22}\frac{\psi}{r} - M_{\theta\theta}^{\mathrm{T}}. \quad (24)$$

Table 1
Imperfection modes.

G1-mode
$a = 0, \ b = 1, \ c = 0.5$

G2-mode
$a = 0, \ b = 3, \ c = 0.5$

G3-mode
$a = 0, \ b = 5, \ c = 0.5$

G4-mode
$a = 0, \ b = 7, \ c = 0.5$

G5-mode
$a = 0, \ b = 9 \ c = 0.5$

G6-mode
$a = 0, \ b = 11, \ c = 0.5$

G7-mode
$a = 0, \ b = 13, \ c = 0.5$

L1-mode
$a = 10, \ b = 1, \ c = 0.5$

L1-mode
$a = 20, \ b = 1, \ c = 0.5$

L1-mode
$a = 30, \ b = 1, \ c = 0.5$

L1-mode
$a = 15, \ b = 1, \ c = 0.3$

L1-mode
$a = 15, \ b = 1, \ c = 0.5$

L1-mode
$a = 15, \ b = 1, \ c = 0.7$

L2-mode
$a = 15, \ b = 3, \ c = 0.5$

L3-mode
$a = 15, \ b = 5, \ c = 0.5$

L4-mode
$a = 15, \ b = 7, \ c = 0.5$

In the above equations, the thermally induced forces (N_{rr}^{T}, $N_{\theta\theta}^{\mathrm{T}}$) and moments ($M_{rr}^{\mathrm{T}}$, $M_{\theta\theta}^{\mathrm{T}}$) are calculated by

$$N_{rr}^{\mathrm{T}} = \sum_{k=1}^{N_L} \int_{z_k}^{z_{k+1}} \left(Q_{11}^{(k)} + Q_{12}^{(k)} \right) \alpha^{(k)} \Delta T \mathrm{d}z,$$
$$N_{\theta\theta}^{\mathrm{T}} = \sum_{k=1}^{N_L} \int_{z_k}^{z_{k+1}} \left(Q_{12}^{(k)} + Q_{22}^{(k)} \right) \alpha^{(k)} \Delta T \mathrm{d}z,$$
(25)

$$M_{rr}^{\mathrm{T}} = \sum_{k=1}^{N_L} \int_{z_k}^{z_{k+1}} z \left(Q_{11}^{(k)} + Q_{12}^{(k)} \right) \alpha^{(k)} \Delta T \mathrm{d}z,$$
$$M_{\theta\theta}^{\mathrm{T}} = \sum_{k=1}^{N_L} \int_{z_k}^{z_{k+1}} z \left(Q_{12}^{(k)} + Q_{22}^{(k)} \right) \alpha^{(k)} \Delta T \mathrm{d}z,$$
(26)

where z_k and z_{k+1} are the coordinates of the upper and lower surfaces, respectively, of the kth GPLRC layer in the thickness direction. The stiffness elements A_{ij} and D_{ij} are defined as

$$\left(A_{ij}, \ D_{ij} \right) = \int_{-h/2}^{h/2} \left(1, z^2 \right) Q_{ij} \mathrm{d}z$$
$$= \sum_{k=1}^{N_L} \int_{z_k}^{z_{k+1}} \left(1, z^2 \right) Q_{ij}^{(k)} \mathrm{d}z, \quad (i, j = 1, 2)$$
(27)

$$A_{55} = \int_{-h/2}^{h/2} Q_{55} \mathrm{d}z = \sum_{k=1}^{N_L} \int_{z_k}^{z_{k+1}} Q_{55}^{(k)} \mathrm{d}z.$$
(28)

Substituting for the force and moment resultants from Eqs. (20)–(24), the governing equations (17)–(19) can be re-expressed in terms of displacement components as

$$A_{11} \left(rU_{,rr} + U_{,r} \right) - A_{22} \frac{U}{r} + \frac{1}{2} \left(A_{11} - A_{12} \right) \left(W_{,r} \right)^2 + \left(A_{11} - A_{12} \right) W_{,r} W_{,r}^*$$
$$+ A_{11} r \left(W_{,rr} W_{,r}^* + W_{,r} W_{,rr}^* + W_{,r} W_{,rr} \right) = 0$$
(29)
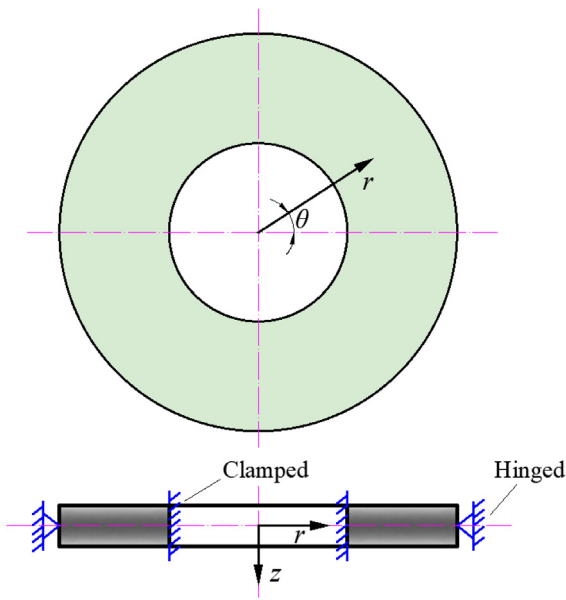
Fig. 2. Support system of the annular plate.

$$A_{55}\left(W_{,r} + \psi\right) + A_{55}r\left(W_{,rr} + \psi_{,r}\right)$$
$$+ \left[A_{11}U_{,r} + \frac{1}{2}A_{11}\left(W_{,r}\right)^2 + A_{11}W_{,r}W_{,r}^* - N_{rr}^{\mathrm{T}}\right]\left(W_{,r} + W_{,r}^*\right)$$
$$+ \left[A_{11}rU_{,rr} + A_{11}rW_{,r}W_{,rr} + A_{11}rW_{,rr}W_{,r}^* + A_{11}rW_{,r}W_{,rr}^* + A_{12}U_{,r}\right]$$
$$\times \left(W_{,r} + W_{,r}^*\right)$$
$$+ \left[A_{11}rU_{,r} + \frac{1}{2}A_{11}r\left(W_{,r}\right)^2 + A_{11}rW_{,r}W_{,r}^* + A_{12}U - rN_{rr}^{\mathrm{T}}\right]$$
$$\times \left(W_{,rr} + W_{,rr}^*\right) = 0$$

(30)

$$D_{11}r\psi_{,rr} + D_{11}\psi_{,r} - D_{22}\frac{\psi}{r} - A_{55}r\left(W_{,r} + \psi\right) = 0. \tag{31}$$

We assume that the annular plate is either clamped (C) or hinged (H) at the edges, as shown in Fig. 2. The corresponding boundary conditions are as follows:

Clamped: $U = 0,\ W = 0,\ \psi = 0$; (32)

Hinged: $U = 0,\ W = 0,\ D_{11}\psi_{,r} + D_{12}\frac{\psi}{r} = 0.$ (33)

2.4. Solution procedure

The GDQ, a robust and efficient numerical method with high accuracy [38,39], is adopted here to solve the governing equations. According to this method, the displacement components and their mth derivatives with respect to r can be approximated as

$$\{U,\ W,\ \psi\}|_{r=r_i} = \sum_{j=1}^{N} l_j(r_i)\left\{U_j,\ W_j,\ \psi_j\right\},$$

$$\frac{\partial^m}{\partial r^m}\{U,\ W,\ \psi\}\bigg|_{r=r_i} = \sum_{j=1}^{N} C_{ij}^{(m)}\left\{U_j,\ W_j,\ \psi_j\right\},$$

(34)

in which $l_j(r)$ are the Lagrange interpolation polynomials; $\{U_j,\ W_j,\ \psi_j\}$ are the values of $\{U,\ W,\ \psi\}$ at $r = r_j$; $C_{(m)}^{ij}$ are the weighting coefficients that can be determined by the recursive formulae [40]. N is the total number of grid points in the x direction generated by a cosine pattern:

$$r_i = R_{\mathrm{b}} + \frac{R_{\mathrm{a}} - R_{\mathrm{b}}}{2}\left[1 - \cos\frac{\pi(i-1)}{N-1}\right],\quad i = 1, 2, \dots, N. \tag{35}$$

Applying the GDQ approximation (34) to the governing equations (29)–(31) leads to a set of nonlinear algebraic equations:

$$A_{11}\left(r_i\sum_{j=1}^{N}C_{ij}^{(2)}U_j + \sum_{j=1}^{N}C_{ij}^{(1)}U_j\right) - A_{22}\frac{U_i}{r_i}$$
$$+ \frac{1}{2}\left(A_{11} - A_{12}\right)\left(\sum_{j=1}^{N}C_{ij}^{(1)}W_j\right)^2 + \left(A_{11} - A_{12}\right)W_{,r}^*\big|_{r=r_i}\sum_{j=1}^{N}C_{ij}^{(1)}W_j$$
$$+ A_{11}r_i\left(W_{,r}^*\big|_{r=r_i}\sum_{j=1}^{N}C_{ij}^{(2)}W_j + W_{,rr}^*\big|_{r=r_i}\sum_{j=1}^{N}C_{ij}^{(1)}W_j\right.$$
$$\left. + \sum_{j=1}^{N}C_{ij}^{(1)}W_j\sum_{j=1}^{N}C_{ij}^{(2)}W_j\right) = 0$$

(36)

$$A_{55}\left(\sum_{j=1}^{N}C_{ij}^{(1)}W_j + \psi_i\right) + A_{55}r_i\left(\sum_{j=1}^{N}C_{ij}^{(2)}W_j + \sum_{j=1}^{N}C_{ij}^{(1)}\psi_j\right)$$
$$+ \left[A_{11}\sum_{j=1}^{N}C_{ij}^{(1)}U_j + \frac{1}{2}A_{11}\left(\sum_{j=1}^{N}C_{ij}^{(1)}W_j\right)^2\right.$$
$$\left. + A_{11}\ W_{,r}^*\big|_{r=r_i}\sum_{j=1}^{N}C_{ij}^{(1)}W_j - N_{rr}^{\mathrm{T}}\right]\left(\sum_{j=1}^{N}C_{ij}^{(1)}W_j + W_{,r}^*\big|_{r=r_i}\right)$$
$$+ \left[A_{11}r_i\sum_{j=1}^{N}C_{ij}^{(2)}U_j + A_{11}r_i\sum_{j=1}^{N}C_{ij}^{(1)}W_j\sum_{j=1}^{N}C_{ij}^{(2)}W_j\right.$$
$$+ A_{11}r_i\ W_{,r}^*\big|_{r=r_i}\sum_{j=1}^{N}C_{ij}^{(2)}W_j + A_{11}r_i\ W_{,rr}^*\big|_{r=r_i}\sum_{j=1}^{N}C_{ij}^{(1)}W_j$$
$$\left. + A_{12}\sum_{j=1}^{N}C_{ij}^{(1)}U_j\right]\left(\sum_{j=1}^{N}C_{ij}^{(1)}W_j + W_{,r}^*\big|_{r=r_i}\right)$$
$$+ \left[A_{11}r_i\sum_{j=1}^{N}C_{ij}^{(1)}U_j + \frac{1}{2}A_{11}r_i\left(\sum_{j=1}^{N}C_{ij}^{(1)}W_j\right)^2\right.$$
$$\left. + A_{11}r_i\ W_{,r}^*\big|_{r=r_i}\sum_{j=1}^{N}C_{ij}^{(1)}W_j + A_{12}U_i - r_iN_{rr}^{\mathrm{T}}\right]\left(\sum_{j=1}^{N}C_{ij}^{(2)}W_j + W_{,rr}^*\big|_{r=r_i}\right)$$
$$= 0$$

(37)

$$D_{11}r_i\sum_{j=1}^{N}C_{ij}^{(2)}\psi_j + D_{11}\sum_{j=1}^{N}C_{ij}^{(1)}\psi_j - D_{22}\frac{\psi_i}{r_i} - A_{55}r_i\left(\sum_{j=1}^{N}C_{ij}^{(1)}W_j + \psi_i\right) = 0. \tag{38}$$

The boundary conditions in Eqs. (32) and (33) can be handled in the same way as

Clamped: $\begin{cases} U_1 = W_1 = \psi_1 = 0 & \text{at } r = r_1, \\ U_N = W_N = \psi_N = 0 & \text{at } r = r_N; \end{cases}$ (39)

Hinged: $\begin{cases} U_1 = W_1 = 0, D_{11}\sum_{j=1}^{N}C_{1j}^{(1)}\psi_j + D_{12}\frac{\psi_1}{r_1} = 0 & \text{at } r = r_1, \\ U_N = W_N = 0, D_{11}\sum_{j=1}^{N}C_{Nj}^{(1)}\psi_j + D_{12}\frac{\psi_N}{r_N} = 0 & \text{at } r = r_N. \end{cases}$ (40)

Keeping Eq. (25) in mind, the governing equations (36)–(38) and the boundary conditions (39) and (40) can be rewritten in a matrix form as

$$\left(\mathbf{K}_{\mathrm{L}} - \Delta T\mathbf{K}_{\mathrm{T}} + \mathbf{K}_{NL1} + \mathbf{K}_{NL2}\right)\mathbf{d} = \mathbf{R}, \tag{41}$$

where $\mathbf{d} = \{\{u_i\},\ \{w_i\},\ \{\varphi_i\}\}^{\mathrm{T}}$ is the unknown displacement vector; $\mathbf{K}_{\mathrm{L}}$, $\mathbf{K}_{\mathrm{T}}$, $\mathbf{K}_{NL1}$, and $\mathbf{K}_{NL2}$ are $3N \times 3N$ stiffness matrices. The elements in $\mathbf{K}_{\mathrm{L}}$ and $\mathbf{K}_{\mathrm{T}}$ are constants, while those in $\mathbf{K}_{NL1}$ and $\mathbf{K}_{NL2}$ are linear and quadratic functions, respectively, of the displacement vector $\mathbf{d}$. $\mathbf{R}$ is a column vector resulting from the temperature rise ΔT and geometric imperfection W^*.

Table 2
Dimensionless postbuckling deflections W_m/R of fully clamped imperfect X-GPLRC annular plates with varying numbers of grid points ($W_{GPL} = 1.0\%$, $R_b/R_a = 0.2$ $R_a/h = 30$, $A_0 = 0.1$, $\Delta T = 80$ K).

N	Imperfection mode							
	G1	G2	G3	G4	L1	L2	L3	L4
9	0.547	0.942	−1.471	1.825	0.711	0.767	0.826	0.785
21	0.545	0.807	−0.379	0.300	0.477	0.429	0.371	0.514
33	0.548	0.811	−0.379	0.280	0.465	0.399	0.278	0.184
45	0.550	0.814	−0.380	0.280	0.466	0.400	0.274	0.162
57	0.550	0.815	−0.379	0.280	0.467	0.400	0.275	0.161
69	0.550	0.814	−0.380	0.280	0.467	0.400	0.275	0.161

For the perfect annular plate, $\mathbf{R}$ and W^* related terms vanish and Eq. (41) reduces to a nonlinear eigenvalue problem, from which the thermal postbuckling equilibrium path can be traced by a direct iteration procedure. By neglecting the nonlinear matrices $\mathbf{K}_{NL1}$ and $\mathbf{K}_{NL2}$, the critical buckling temperature rise can be obtained through a standard eigenvalue algorithm as well. For the imperfect annular plate, $\mathbf{R}$ is nonzero and the bifurcation buckling does not exist. In this case, the postbuckling load–deflection curve can be determined by the modified Newton–Raphson procedure as detailed by Zou and Lam [41].

3. Numerical results and discussion

In what follows, the FG-GPLRC annular plates of thickness $h = 0.01$ m and layer number $N_L = 10$ are considered, and the annular plates are a mixture of epoxy and GPLs with material properties: $E_m = 3.0$ GPa, $\rho_m = 1200$ kg/m^3, $v_m = 0.34$, $\alpha_m = 6.0 \times 10^{-5}$/K; $E_{GPL} = 1.01$ TPa, $\rho_{GPL} = 1062.5$ kg/m^3, $v_{GPL} = 0.186$, $\alpha_{GPL} = 5.0 \times 10^{-6}$/K, $d_{GPL} = 1 \mu$m, $t_{GPL} = 1$ nm. Numerical results of axisymmetric thermal postbuckling are presented for both perfect and imperfect FG-GPLRC annular plates to highlight the influences of various geometric imperfections. Unless otherwise specified, the imperfection parameters for L1-mode are $a = 15$, $b = 1$, and $c = 0.5$. Thermal buckling results of perfect annular plates are also provided as a subset problem.

3.1. Convergence and validation

Convergence and validation studies are first conducted to ensure the accuracy of the present formulation and solution procedure. Table 2 tabulates the dimensionless postbuckling deflections of fully clamped imperfect X-GPLRC annular plates with varying numbers of grid points at the temperature rise $\Delta T = 80$ K. W_m/R denotes the maximum dimensionless deflection. It is found that the solutions become convergent when the number of grid points is increased to 57. Hence, $N = 57$ are used in all the following examples.

Thermal buckling temperature parameters of simply supported isotropic homogeneous annular plates are calculated and compared in Table 3 with those of Wang et al. [42] and Sepahi et al. [43]. Three different inner-to-outer radius ratios ($R_b/R_a = 0.2, 0.4, 0.6$) and radius-to-thickness ratios ($R_a/h = 5, 10, 20$) are considered in this example. As can be seen, our results agree very well with those in the literature.

As there are no suitable results on thermal postbuckling of imperfect annular plates for comparison, the present results are validated against the finite element results obtained by using ABAQUS. To begin with, the imperfect annular plate model is created in Solidworks and then is imported into ABAQUS. Subsequently, the annular plate is divided into ten layers with different material properties by the "*create composite layup*" option and meshed with eight-node quadratic reduced integration shell (S8R) elements with controlled size. At last, the "*Static, Risk*" solver is adopted to obtain the thermal postbuckling equilibrium path. Fig. 3 compares thermal postbuckling results obtained by the GDQ method and ABAQUS for globally imperfect X-GPLRC annular plates. Two boundary conditions, i.e., H-H and C-C, are taken into account. The comparison study shows that the present results are in excellent
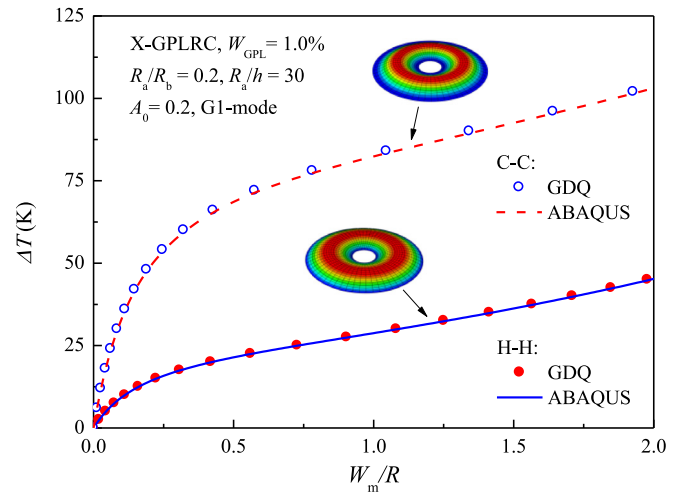

Fig. 3. Comparison of thermal postbuckling equilibrium paths for imperfect X-GPLRC annular plates.

agreement with those obtained by ABAQUS, and both H-H and C-C imperfect annular plates possess axisymmetric thermal postbuckling shapes.

3.2. Thermal buckling

This section investigates the influences of GPL parameters (distribution pattern, weight fraction and dimension), plate geometry parameters (radius-to-thickness ratio and inner-to-outer radius ratio) on the thermal buckling of perfect FG-GPLRC annular plates. As the axisymmetric problem is considered in the present study, only the H-H annular plate which exhibits an axisymmetric buckling shape is discussed in this section.

Table 4 lists the thermal buckling results of perfect H-H X-GPLRC annular plates with different geometry parameters. The results obtained by ABAQUS are given as well to further demonstrate the accuracy of the present solution procedure. Again, a close agreement is achieved. Both the present results and those obtained by ABAQUS show that the buckling temperature rise grows as the inner-to-outer radius ratio R_b/R_a increases, but the increase percentage is hardly affected by the radius-to-thickness ratio R_a/h. On the other hand, the buckling temperature rise significantly decreases as the radius-to-thickness ratio increases, and the decrease percentage remains almost constant for different inner-to-outer radius ratios. For example, thermal buckling temperature rise is decreased by around 84% when the radius-to-thickness ratio is increased from 20 to 50 for all values of R_b/R_a. In summary, the thick plate with a shorter span possesses a higher stiffness and therefore has a greater thermal buckling resistance.

Figs. 4 and 5 illustrate the effects of GPL weight fraction W_{GPL} and diameter-to-thickness ratio d_{GPL}/t_{GPL} on the thermal buckling of H-H FG-GPLRC annular plates with different GPL distribution patterns. As can be seen, the buckling temperature rise of the X-GPLRC annular plate grows as either the GPL concentration or the diameter-to-thickness ratio increases, while that of the O-GPLRC annular plate exhibits a completely opposite changing trend. However, these effects become less pronounced when the values of W_{GPL} and d_{GPL}/t_{GPL} are sufficiently large. In contrast, the buckling temperature rise of the U-GPLRC annular plate keeps nearly constant. This can be explained by Eq. (25) that greater values of W_{GPL} and d_{GPL}/t_{GPL} increase both elastic stiffness Q_{ij} and thermal buckling load (N_{rr}^T, $N_{\theta\theta}^T$), but does not necessarily lead to a higher buckling temperature rise.

Table 3

Comparison of thermal buckling temperature parameters $\lambda_T = 12(1+\nu)\alpha\Delta T_{cr}(R_a/h)^2$ for simply supported isotropic homogeneous annular plates.

R_a/h	$R_b/R_a = 0.2$			$R_b/R_a = 0.4$			$R_b/R_a = 0.6$		
	Present	Ref. [42]	Ref. [43]	Present	Ref. [42]	Ref. [43]	Present	Ref. [42]	Ref. [43]
20	18.543	18.542	18.547	28.634	28.633	28.642	60.164	60.187	60.199
10	17.712	17.724	17.725	26.893	26.915	26.921	53.144	53.246	53.252
5	15.030	15.070	15.070	21.636	21.706	21.709	36.235	36.433	36.437

Table 4

Thermal buckling temperature rise ΔT_{cr} (K) of perfect H-H X-GPLRC annular plates with different geometry parameters ($W_{GPL} = 1.0\%$).

R_a/h	Source	R_b/R_a				
		0.1	0.2	0.3	0.4	0.5
20	GDQ	57.38	61.16	73.14	94.45	130.9
	ABAQUS	56.97	60.86	72.80	93.91	129.9
30	GDQ	25.83	27.50	32.92	42.66	59.48
	ABAQUS	25.73	27.45	32.88	42.59	59.33
40	GDQ	14.60	15.53	18.60	24.13	33.72
	ABAQUS	14.56	15.51	18.58	24.08	33.63
50	GDQ	9.362	9.959	11.93	15.48	21.66
	ABAQUS	9.352	9.950	11.92	15.47	21.62
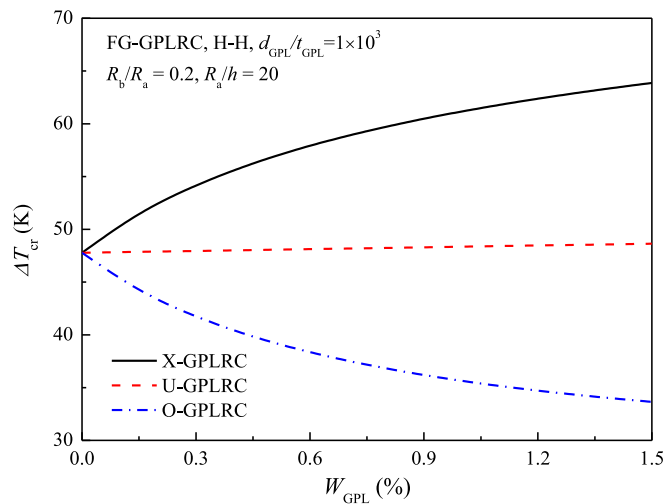
Fig. 4. Effect of GPL weight fraction on thermal buckling of FG-GPLRC annular plates.
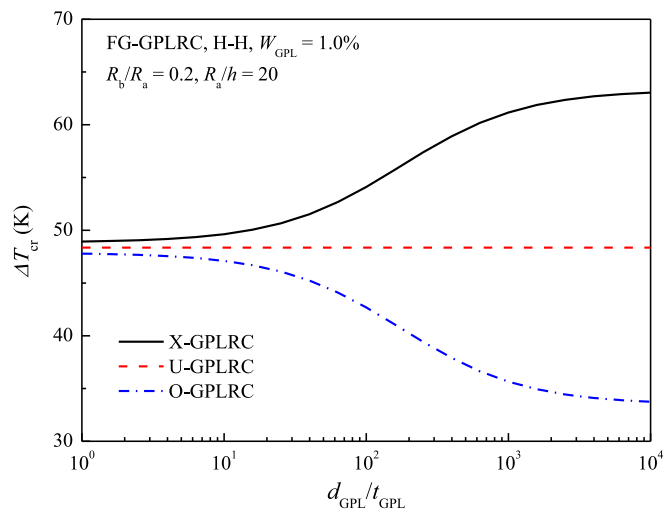
Fig. 5. Effect of GPL diameter-to-thickness ratio on thermal buckling of FG-GPLRC annular plates.
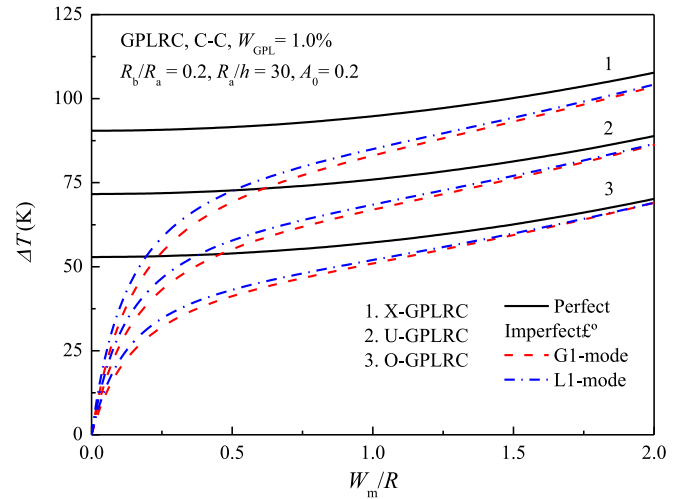

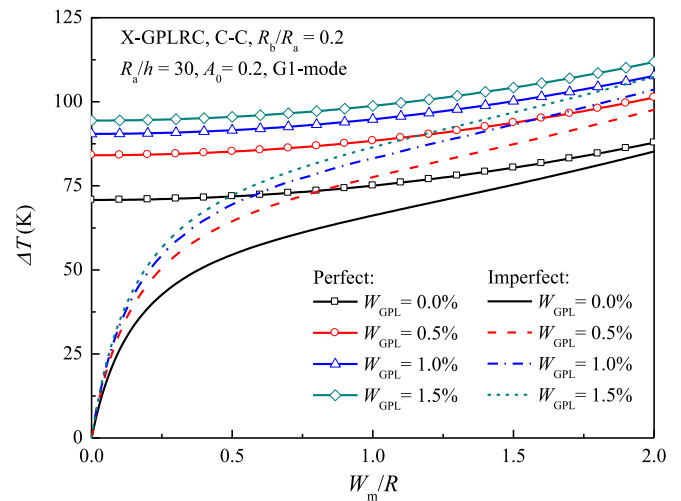**Fig. 6.** Effect of GPL distribution pattern on thermal postbuckling of FG-GPLRC annular plates.

Fig. 7. Effect of GPL weight fraction on thermal postbuckling of FG-GPLRC annular plates.

3.3. Thermal postbuckling

In this section, thermal postbuckling results, in the form of postbuckling temperature rise ΔT (K) plotted versus the dimensionless maximum deflection W_m/R, are presented for imperfect FG-GPLRC annular plates with various geometric imperfections. As the thermal postbuckling shapes of imperfect annular plates are axisymmetric (see Fig. 3), the axisymmetric results of their perfect counterparts are also given as the reference to evaluate the influences of various imperfection parameters on the thermal postbuckling.

Fig. 6 depicts the thermal postbuckling equilibrium paths of perfect and imperfect FG-GPLRC annular plates with different GPL distribution patterns. The global and localized imperfections (G1- and L1-modes)
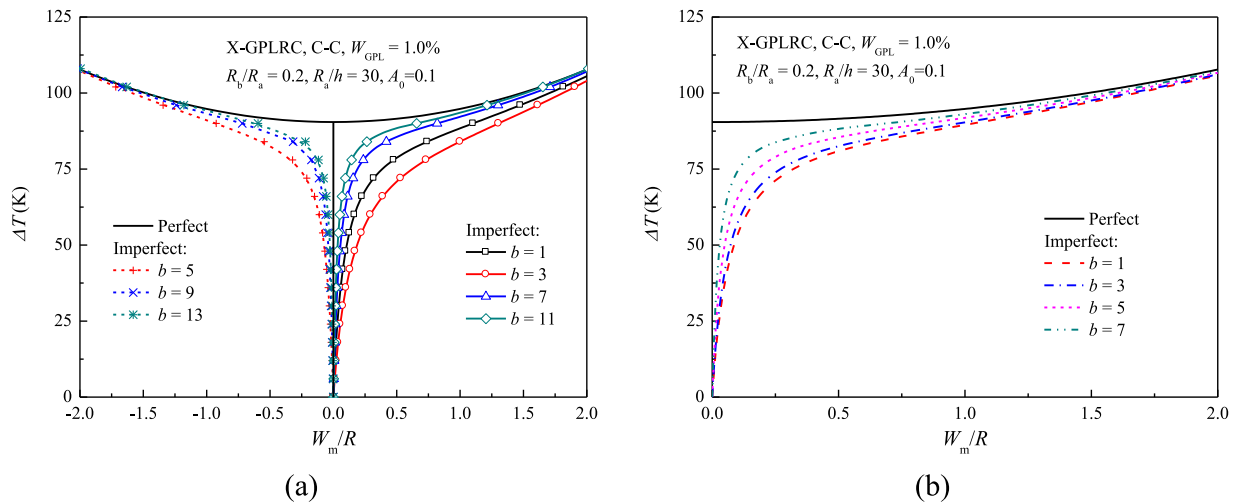
Fig. 8. Effect of half-wave number on thermal postbuckling of FG-GPLRC annular plates with (a) global and (b) localized imperfections.

are considered in this case. It shows that pattern X gives the highest thermal postbuckling resistance, then the pattern U and O. The thermal postbuckling curves are weakened due to the existence of imperfections, with the influence of G1-mode being slightly obvious than that of L1-mode.

Fig. 7 displays the effect of GPL weight fraction on the thermal postbuckling of X-GPLRC annular plates with a G1-mode imperfection. The thermal postbuckling resistance of the X-GPLRC annular plate is enhanced as the GPL concentration increases, but its sensitivity to the imperfection is hardly affected. It is similar to the observation in thermal buckling that the thermal postbuckling temperatures of O- and U-GPLRC annular plates are decreased and remain unchanged, respectively, and thus are omitted here.

The influence of half-wave number on the thermal postbuckling of X-GPLRC annular plates is investigated in Figs. 8(a) and (b) where the global and localized imperfections are considered, respectively. Overall, the thermal postbuckling curves of imperfect annular plates get gradually closer to that of the perfect counterparts as the half-wave number grows. It is noteworthy that negative deflections occurs when the half-wave number of global imperfections $b = 5, 9, 13$, etc., which implies that the globally imperfect annular plates are likely to deflect towards the side with few half-waves (excluding $b = 1$), as shown in Table 1. Comparing the curves in Figs. 8(a) and (b) shows that the thermal postbuckling curve is more sensitive to the global imperfections than the localized ones.

Figs. 9 and 10 evaluate the effects of imperfection location and localization degree on the thermal postbuckling of X-GPLRC plates containing a L1-mode imperfection, respectively. As indicated in Table 1, a smaller/larger value of c means that the imperfection amplitude is closer to the inner/outer edge of the annular plate, while $c = 0.5$ implies the imperfection is symmetric about the midspan $r = (R_a + R_b)/2$. In addition, a greater value of a indicates a narrower imperfection shape, and $a = 0$ means the localized imperfection is reduced to the global one. It is seen from Fig. 9 that the thermal postbuckling curve is most lowered when the imperfection amplitude is located at the midspan ($c = 0.5$), and negative deflection occurs when the imperfection is close to the edges. Fig. 10 shows that the thermal postbuckling equilibrium path of the imperfect annular plate become closer to that of the perfect counterpart as the localization degree increases, which demonstrates that the thermal postbuckling behaviour is less sensitive to the imperfection with a narrow shape.

Fig. 11 examines the effect of imperfection amplitude on the thermal postbuckling of X-GPLRC annular plates with G1- and L1-mode imperfections. It shows that a larger imperfection amplitude leads to a lower thermal postbuckling resistance, but this influence seems to be less significant when the amplitude further grows.
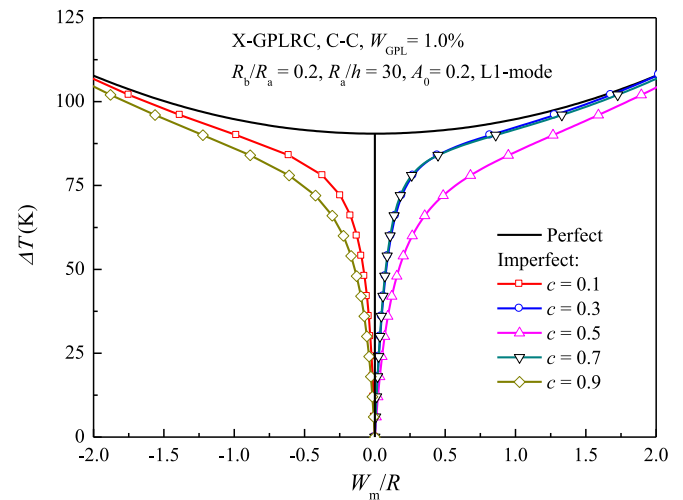

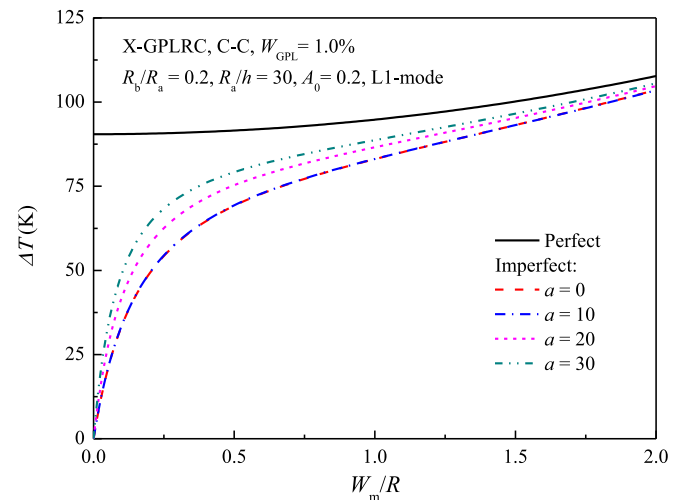**Fig. 9.** Effect of imperfection location on thermal postbuckling of FG-GPLRC annular plates.

Fig. 10. Effect of imperfection localization degree on thermal postbuckling of FG-GPLRC annular plates.
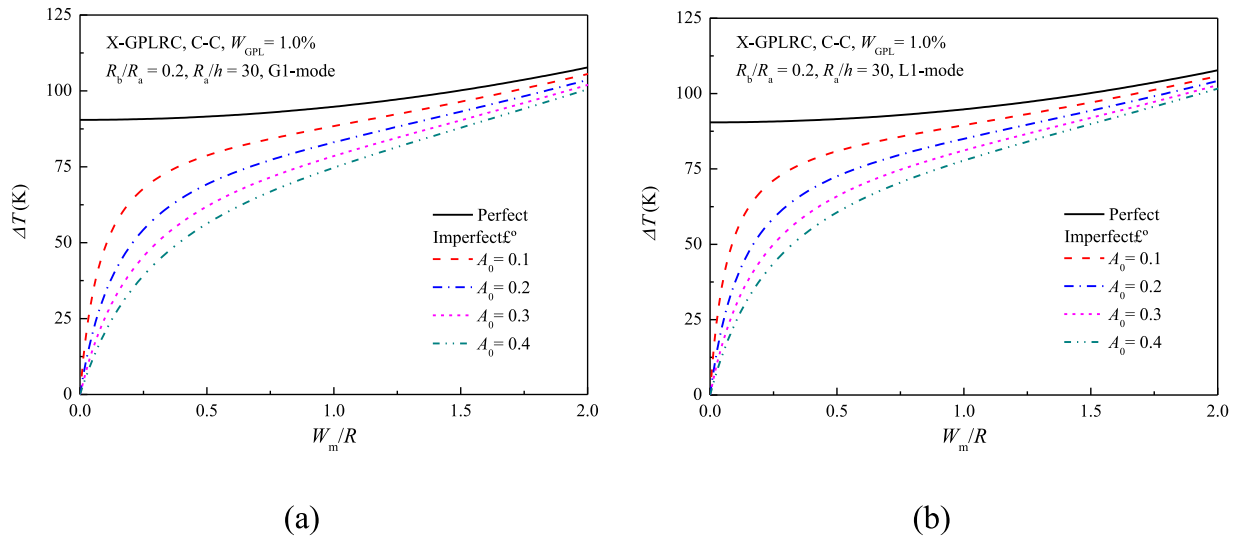
Fig. 11. Effect of imperfection amplitude on thermal postbuckling of FG-GPLRC annular plates: (a) G1-mode; (b) L1-mode.
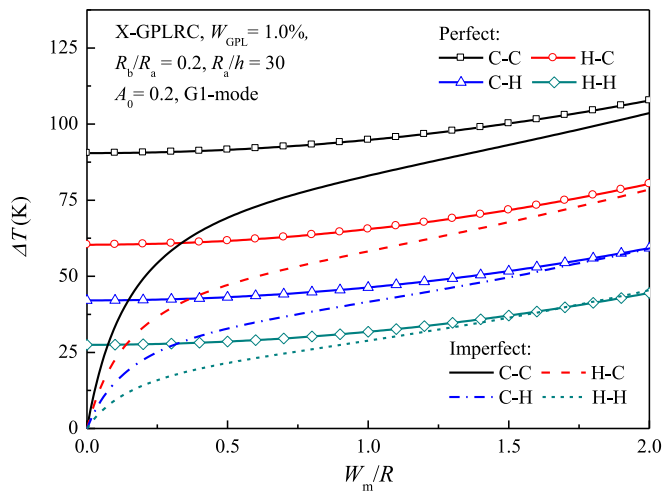

Fig. 12. Effect of boundary conditions on thermal postbuckling of FG-GPLRC annular plates.

The effects of boundary conditions and geometry parameters on the thermal postbuckling of X-GPLRC annular plates with a G1-mode imperfection are studied in Figs. 12 and 13, respectively. It is found that the fully clamped thick annular plate with a smaller inner-to-outer radius ratio exhibits a higher thermal postbuckling strength. Comparing the difference between the curves in both figures shows that the imperfection sensitivity of thermal postbuckling is relatively increased by using rigid end supports but is hardly affected by geometry parameters.

It is observed in all figures that the thermal postbuckling curves of imperfect annular plates become very close to those of their perfect counterparts at a larger deflection, this is because with the deflection increasing, the nonlinear stiffness associated with displacements turns to be the main influential factor of thermal postbuckling.

4. Conclusion

This paper for the first time investigates the sensitivity of axisymmetric thermal postbuckling of FG-GPLRC annular plates to various geometric imperfections. A theoretical model is established within the framework of FSDT and von Kármán geometric nonlinearity, and an efficient numerical solution procedure is developed based on the GDQ method and modified Newton–Raphson iteration technique. The present formulations and solution procedure are verified by comparing the present results with those in the literature and obtained by ABAQUS. Tabular and graphical results are presented to examine the influences of GPL distribution pattern, concentration and dimension, imperfection mode, amplitude, location and localization degree, plate geometry, as well as boundary conditions on the thermal postbuckling behaviour of FG-GPLRC annular plates. The main findings are concluded as follows:

(1) Whether the thermal buckling and postbuckling resistance of FG-GPLRC annular plates is increased or decreased with the GPL concentration and diameter-to-thickness ratio is dependent on the GPL distribution pattern.

(2) The thermal postbuckling resistance of FG-GPLRC annular plates is weakened due to the existence of geometric imperfections, and is more reduced by the global imperfections than the localized ones.

(3) The effect of geometric imperfections on the thermal postbuckling becomes less significant as the half-wave number grows, and the globally imperfect annular plate is inclined to deflect towards the side with fewer half-waves.

(4) The thermal postbuckling path is most lowered when the localized imperfection is symmetric about the midspan, and negative deflections occur when the imperfection is located near the annular plate edges.

(5) The thermal postbuckling resistance become less sensitive to the imperfections with a narrower shape, but is considerably reduced when the imperfection amplitude increases.

(6) The sensitivity of thermal postbuckling to geometric imperfections is moderately affected by boundary conditions, but is hardly influenced by the annular plate geometry.

The theoretical model and solution procedure developed in this paper are beneficial to accurate prediction of thermal postbuckling of FG-GPLRC annular plates with geometric imperfections. Moreover, the obtained results and main findings will serve to better understand the thermal postbuckling behaviours of geometrically imperfect FG-GPLRC annular plates and contribute to their practical design and applications in structural engineering. On the other hand, only the axisymmetric geometric imperfections are considered in the current study, which restricts the present formulation and solution method to the axisymmetric thermal buckling and postbuckling problems. With this in mind, further researches can be carried out in the near future by relaxing the axisymmetric assumption and considering more general geometric imperfections with asymmetric shapes.
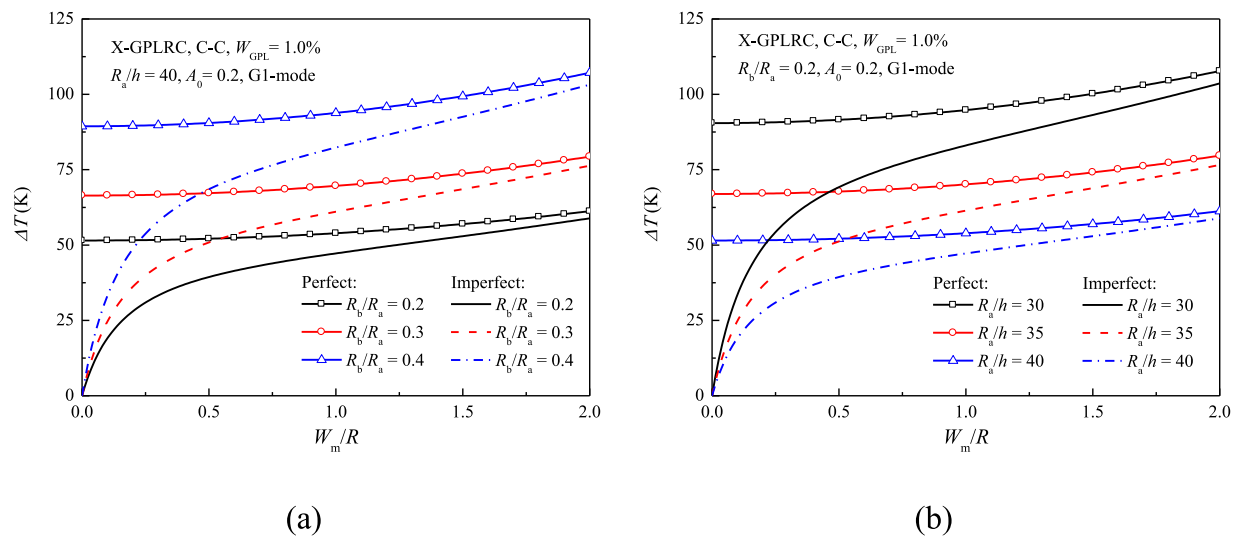
Fig. 13. Effect of geometry parameters on thermal postbuckling of FG-GPLRC annular plates: (a) R_b/R_a; (b) R_a/h.

CRediT authorship contribution statement

Helong Wu: Writing – original draft, Methodology, Funding acquisition, Conceptualization. **Ziqiang Zheng:** Investigation, Formal analysis. **Jing Guo:** Validation, Investigation. **Long Li:** Methodology, Conceptualization. **Yumei Bao:** Writing – review & editing. **Jie Yang:** Writing – review & editing, Supervision.

Declaration of competing interest

The authors declare that they have no known competing financial interests or personal relationships that could have appeared to influence the work reported in this paper.

Data availability

Data will be made available on request.

Acknowledgements

References

[1] S. Zhao, Z. Zhao, Z. Yang, L. Ke, S. Kitipornchai, J. Yang, Functionally graded graphene reinforced composite structures: A review, Eng. Struct. 210 (2020) 110339.

[2] J. Yang, H. Wu, S. Kitipornchai, Buckling and postbuckling of functionally graded multilayer graphene platelet-reinforced composite beams, Compos. Struct. 161 (2017) 111–118.

[3] M. Song, S. Kitipornchai, J. Yang, Free and forced vibrations of functionally graded polymer composite plates reinforced with graphene nanoplatelets, Compos. Struct. 159 (2017) 579–588.

[4] C. Feng, S. Kitipornchai, J. Yang, Nonlinear bending of polymer nanocomposite beams reinforced with non-uniformly distributed graphene platelets (GPLs), Composites B 110 (2017) 132–140.

[5] Z. Yang, Y. Huang, A. Liu, J. Fu, D. Wu, Nonlinear in-plane buckling of fixed shallow functionally graded graphene reinforced composite arches subjected to mechanical and thermal loading, Appl. Math. Model. 70 (2019) 315–327.

[6] Z. Yang, A. Liu, S.-K. Lai, B. Safaei, J. Lv, Y. Huang, J. Fu, Thermally induced instability on asymmetric buckling analysis of pinned-fixed FG–GPLRC arches, Eng. Struct. 250 (2022) 113243.

[7] S. Kitipornchai, D. Chen, J. Yang, Free vibration and elastic buckling of functionally graded porous beams reinforced by graphene platelets, Mater. Des. 116 (2017) 656–665.

[8] H.-S. Shen, F. Lin, Y. Xiang, Nonlinear bending and thermal postbuckling of functionally graded graphene-reinforced composite laminated beams resting on elastic foundations, Eng. Struct. 140 (2017) 89–97.

[9] H. Wu, J. Yang, S. Kitipornchai, Dynamic instability of functionally graded multilayer graphene nanocomposite beams in thermal environment, Compos. Struct. 162 (2017) 244–254.

[10] Z. Zhang, Y. Li, H. Wu, H. Zhang, H. Wu, S. Jiang, G. Chai, Mechanical analysis of functionally graded graphene oxide-reinforced composite beams based on the first-order shear deformation theory, Mech. Adv. Mater. Struct. 27 (1) (2020) 3–11.

[11] R. Gholami, R. Ansari, Large deflection geometrically nonlinear analysis of functionally graded multilayer graphene platelet-reinforced polymer composite rectangular plates, Compos. Struct. 180 (2017) 760–771.

[12] H. Wu, J. Yang, S. Kitipornchai, Parametric instability of thermo-mechanically loaded functionally graded graphene reinforced nanocomposite plates, Int. J. Mech. Sci. 135 (2018) 431–440.

[13] K. Gao, W. Gao, D. Chen, J. Yang, Nonlinear free vibration of functionally graded graphene platelets reinforced porous nanocomposite plates resting on elastic foundation, Compos. Struct. 204 (2018) 831–846.

[14] B. Saiah, M. Bachene, M. Guemana, Y. Chiker, B. Attaf, On the free vibration behavior of nanocomposite laminated plates contained piece-wise functionally graded graphene-reinforced composite plies, Eng. Struct. 253 (2022) 113784.

[15] D. Liu, S. Kitipornchai, W. Chen, J. Yang, Three-dimensional buckling and free vibration analyses of initially stressed functionally graded graphene reinforced composite cylindrical shell, Compos. Struct. 189 (2018) 560–569.

[16] M. Sobhy, Magneto-electro-thermal bending of FG-graphene reinforced polymer doubly-curved shallow shells with piezoelectromagnetic faces, Compos. Struct. (2018).

[17] Z. Qin, S. Zhao, X. Pang, B. Safaei, F. Chu, A unified solution for vibration analysis of laminated functionally graded shallow shells reinforced by graphene with general boundary conditions, Int. J. Mech. Sci. 170 (2020) 105341.

[18] M.T. Song, J. Yang, S. Kitipornchai, W.D. Zhu, Buckling and postbuckling of biaxially compressed functionally graded multilayer graphene nanoplatelet-reinforced polymer composite plates, Int. J. Mech. Sci. 131 (2017) 345–355.

[19] H. Wu, S. Kitipornchai, J. Yang, Thermal buckling and postbuckling of functionally graded graphene nanocomposite plates, Mater. Des. 132 (2017) 430–441.

[20] V. Nguyen Van Do, C.-H. Lee, Isogeometric analysis for buckling and postbuckling of graphene platelet reinforced composite plates in thermal environments, Eng. Struct. 244 (2021) 112746.

[21] M. Shakouri, A. Mohseni, Buckling analysis of rectangular sandwich plates with functionally graded graphene-reinforced face layers, J. Braz. Soc. Mech. Sci. 42 (10) (2020) 540.

[22] H.-S. Shen, Y. Xiang, F. Lin, D. Hui, Buckling and postbuckling of functionally graded graphene-reinforced composite laminated plates in thermal environments, Composites B 119 (2017) 67–78.

[23] H.-S. Shen, Y. Xiang, F. Lin, Thermal buckling and postbuckling of functionally graded graphene-reinforced composite laminated plates resting on elastic foundations, Thin-Walled Struct. 118 (2017) 229–237.

[24] Y. Kiani, NURBS-based isogeometric thermal postbuckling analysis of temperature dependent graphene reinforced composite laminated plates, Thin-Walled Struct. 125 (2018) 211–219.

[25] B. Yang, S. Kitipornchai, Y.-F. Yang, J. Yang, 3D thermo-mechanical bending solution of functionally graded graphene reinforced circular and annular plates, Appl. Math. Model. 49 (2017) 69–86.

[26] D. Liu, Z. Li, S. Kitipornchai, J. Yang, Three-dimensional free vibration and bending analyses of functionally graded graphene nanoplatelets-reinforced nanocomposite annular plates, Compos. Struct. 229 (2019) 111453.

[27] H. Wu, J. Zhu, S. Kitipornchai, Q. Wang, L.-L. Ke, J. Yang, Large amplitude vibration of functionally graded graphene nanocomposite annular plates in thermal environments, Compos. Struct. 239 (2020) 112047.

[28] P. Malekzadeh, A. Setoodeh, M. Shojaee, Vibration of FG–GPLs eccentric annular plates embedded in piezoelectric layers using a transformed differential quadrature method, Comput. Method Appl. M 340 (2018) 451–479.

[29] Y. Yang, B. Chen, W. Lin, Y. Li, Y. Dong, Vibration and symmetric thermal buckling of asymmetric annular sandwich plates with piezoelectric/GPLRC layers rested on foundation, Aerosp. Sci. Technol. 110 (2021) 106495.

[30] J. Zheng, C. Zhang, A. Khan, T.A. Sebaey, N. Farouk, On the asymmetric thermal stability of FGM annular plates reinforced with graphene nanoplatelets, Eng. Comput. (2021).

[31] Y. Yang, Q. Luo, J.-a. Li, Y. Dong, B. Chen, Y. Li, Symmetric and asymmetric thermo-induced buckling and postbuckling of rotating GPLRC annular plates rested on elastic foundation, Eng. Struct. 259 (2022) 114110.

[32] Z.-M. Li, P. Qiao, Buckling and postbuckling behavior of shear deformable anisotropic laminated beams with initial geometric imperfections subjected to axial compression, Eng. Struct. 85 (2015) 277–292.

[33] H.L. Wu, J. Yang, S. Kitipornchai, Nonlinear vibration of functionally graded carbon nanotube-reinforced composite beams with geometric imperfections, Composites B 90 (2016) 86–96.

[34] H. Wu, S. Kitipornchai, J. Yang, Free vibration of thermo-electro-mechanically postbuckled FG–CNTRC beams with geometric imperfections, Steel Compos Struct 29 (3) (2018) 319–332.

[35] H. Wu, Y. Li, L. Li, S. Kitipornchai, L. Wang, J. Yang, Free vibration analysis of functionally graded graphene nanocomposite beams partially in contact with fluid, Compos. Struct. 291 (2022) 115609.

[36] J. Halpin, J. Kardos, The Halpin–Tsai equations: A review, Polym. Eng. Sci. 16 (5) (1976) 344–352.

[37] M.A. Van Es, Polymer-Clay Nanocomposites: The Importance of Particle Dimensions, Delft University of Technology, 2001.

[38] C. Shu, Generalized Differential-Integral Quadrature and Application to the Simulation of Incompressible Viscous Flows Including Parallel Computation, University of Glasgow, United Kingdom, 1991.

[39] C. Shu, B.E. Richards, Application of generalized differential quadrature to solve two-dimensional incompressible Navier–Stokes equations, Int. J. Numer. Methods Fluids 15 (7) (1992) 791–798.

[40] C. Shu, Y. Chew, Application of multi-domain GDQ method to analysis of waveguides with rectangular boundaries, Prog. Electromagn. Res. 21 (1999) 1–19.

[41] G. Zou, S. Lam, Post-buckling analysis of imperfect laminates using finite strips based on a higher-order plate theory, Int. J. Numer. Methods Eng. 56 (15) (2003) 2265–2278.

[42] C.M. Wang, Y. Xiang, S. Kitipornchai, K.M. Liew, Buckling solutions for Mindlin plates of various shapes, Eng. Struct. 16 (2) (1994) 119–127.

[43] O. Sepahi, M.R. Forouzan, P. Malekzadeh, Thermal buckling and postbuckling analysis of functionally graded annular plates with temperature-dependent material properties, Mater. Des. 32 (7) (2011) 4030–4041.